ACS APPLIED NANO MATERIALS

www.acsanm.org Article

Near-Infrared Laser-Responsive Erythrocyte Membrane Camouflaged Nanoparticles for Chemo-Photodynamic Therapy of Breast Cancer

Qingran Guan,[§] Jianshuo Su,[§] Yinglan Li, Huaizhen Zhang, Zhuang Ding, Qingpeng Wang, Shilei Ji, Jun Han, Min Liu,* and Yanna Zhao*

Cite This: https://doi.org/10.1021/acsanm.4c02669 Read Online

ACCESS | Metrics & More | Article Recommendations | Supporting Information

ABSTRACT: The effectiveness of chemotherapy as a primary approach in cancer treatment is under scrutiny due to the rise of multidrug resistance (MDR). Biomimetic technology presents numerous opportunities for the development of therapeutic platforms that exhibit enhanced performance in antitumor therapy and address the limitations of traditional chemotherapy. In this study, an erythrocyte membrane (EM)-camouflaged biomimetic nanodrug delivery platform, namely B-Lip@PTX/Cur/Ce6, capable of simultaneously delivering paclitaxel (PTX, a chemotherapeutic agent), curcumin (Cur, a P-gp inhibitor), and chlorin e6 (Ce6, a photosensitizer), was introduced for synergistic chemo-photodynamic therapy. With near-infrared laser irradiation, B-Lip@PTX/Cur/Ce6 has been found to induce the production of reactive oxygen species (ROS), thereby triggering both photodynamic therapy (PDT) and hybrid cell membrane disruption for controlled release of PTX/Cur. Furthermore, in vitro cytotoxicity has demonstrated the ability of Cur in B-Lip@PTX/Cur/Ce6 to reverse MDR by enhancing the inhibitory impact of PTX on MCF-7/ADR cells. By employing the EM coating strategy, B-Lip@PTX/Cur/Ce6 could demonstrate favorable biocompatibility, while also exhibiting prolonged circulation time in the bloodstream, which would be beneficial to long-term accumulation at the tumor sites. Notably, the innovative biomimetic platform demonstrates successful inhibition of MDR and exhibits efficacy in combating tumors through enhanced chemo-photodynamic therapy. The integration of the versatile nanoscopic drug delivery system results in an augmentation of the therapeutic activity against cancer and holds promising potential for treating breast cancer effectively.

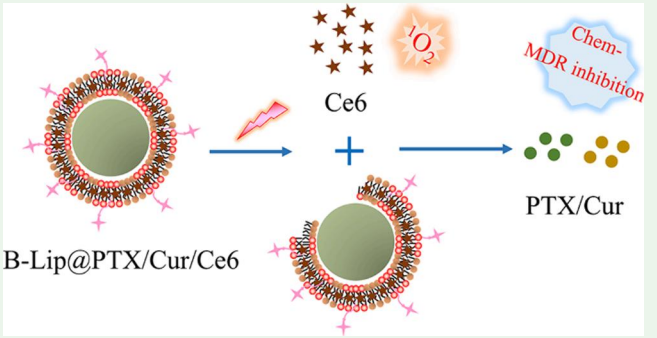

KEYWORDS: *chemo-photodynamic therapy, MDR inhibition, Laser-responsive release, erythrocyte membrane biomimetic, self-assembly mechanism*

1. INTRODUCTION

Breast cancer is a prominent global health concern, ranking as the primary cause of malignant tumors, as well as exhibiting the highest incidence and mortality rates among females. Consequently, it has emerged as a significant challenge for women in contemporary society.[1] Chemotherapy, a widely employed clinical cancer therapy strategy, holds considerable potential for eradicating rapidly dividing tumor cells and impeding tumor progression, particularly in breast cancer patients. Currently, the majority of chemotherapeutic agents exhibit limited solubility in water and lack the ability to selectively target tumor cells for complete eradication, thereby posing a significant challenge in the field of chemotherapy.[2,3] Besides, the efficacy of chemotherapy in this context is significantly impeded by MDR.[4−6] In contemporary pharmaceutical research, a potential solution lies in the exploration of combination therapy, which involves the simultaneous administration of multiple antitumor medications or treatments. This approach aims to achieve codelivery of these drugs within cancer cells, thereby enhancing their efficacy through a synergistic effect, in which chemotherapy exhibits strong synergistic effects with other therapies and serves as a powerful adjunct to them.[7] Consequently, a potentially fruitful approach for cancer treatment could entail investigating drug formulations capable of reversing resistance to chemotherapeutic agents in patients, while simultaneously enhancing the biocompatibility and biosafety of such formulations and

Received: May 8, 2024
Revised: May 13, 2024
Accepted: May 15, 2024

augmenting the therapeutic efficacy of chemotherapeutic drugs against tumors.

Photodynamic therapy (PDT) has received approval from the FDA Center as an advanced therapeutic strategy for combating tumors clinically.[8,9] PDT offers minimal invasiveness, precise spatiotemporal control, strong selectivity for tumor tissues, and reduced sensitivity to MDR.[10−12] By subjecting the photosensitizers to laser irradiation at specific wavelength, they are excited to their triplet state, resulting in the production of reactive oxygen species (ROS), such as singlet oxygen ($^1O_2$), through energy conversion with the surrounding molecular oxygen. These species exhibit hypercytotoxicity against cancer cells.[13] However, PDT alone does not achieve complete eradication of cancer cells due to its limited penetration depths and the high likelihood of local cancer recurrence.[14] Previous research, including our own, has demonstrated the successful utilization of photosensitizers in combination with chemotherapy, resulting in desirable synergistic anticancer effects.[15,16]

Multiple mechanisms contribute to the development of MDR and the mechanism involving p-glycoprotein (P-gp) efflux pumps has been extensively studied.[17,18] To combat drug resistance and enhance the efficacy of antitumor chemotherapeutic agents, downregulation of substances such as P-gp inhibitors is employed. Typically, combining chemotherapy agents with P-gp inhibitors has been identified as a promising approach to effectively combat MDR, leading to substantial improvements in anticancer efficacy and reduced toxicity.[19−22] In addition, the coadministration of chemotherapeutic drugs with P-gp inhibitors using one single delivery system to the tumor site has been verified to augment their therapeutic effectiveness.[23]

However, due to the distinct physicochemical properties and in vivo behavior of chemotherapeutic and photodynamic agents, as well as P-gp inhibitors, ensuring their consistent aggregation at the tumor site and maintaining consistent pharmacological processes in vivo pose a challenge. Nanodrug delivery systems have been recognized as potential strategies for the treatment of breast carcinoma due to their ability to facilitate coloaded delivery and precisely controlled release of multiple drugs. The combination approach is considered rational and viable, aiming to achieve the most effective therapeutic outcome. Furthermore, in cancer therapy, the overarching objective of a nanodrug delivery system is to augment the therapeutic efficacy of anticancer agents and mitigate their adverse impacts by optimizing drug encapsulation, minimizing drug leakage, evading immune system clearance, and ultimately enabling precise transportation, together with continuous release of drugs at the tumor site. In recent years, many studies have indicated the potential of biomimetic drug delivery systems to effectively load both small- and large-molecule drugs for tumor treatment, as well as be utilized for multifunctional nanoagents.[24,25] Consequently, an integrated biomimetic nanoplatform that combines chemo-photodynamic therapy with P-gp inhibitors may represent the most advantageous approach for treating male breast cancer in a clinical setting. A red blood cell (RBC)-derived erythrocyte membrane with various advantageous biological characteristics has been recognized as a significant benchmark for innovative nanocarriers.[26−28] Acting as a biomimetic coating, an erythrocyte membrane aids nanoparticles in evading immune system clearance within the body, diminishing blood clearance, prolonging in vivo circulation time, and exhibiting more favorable pharmacokinetic properties linked to the medication, which hold great importance for clinical applications.[24,29−31]

In this particular study, erythrocyte membrane-camouflaged carrier-free nanoparticles were developed to simultaneously deliver the photosensitizer chlorin e6 (Ce6), the chemotherapeutic agent paclitaxel (PTX), and the P-gp inhibitor curcumin (Cur) (Scheme 1) for combining chemo-photodynamic therapy with MDR inhibition, thus restraining proliferation in breast cancer. PTX and Cur were self-assembled into carrier-free nanocrystals (PTX/Cur NCs) by a solvent exchange method, which were then coated by erythrocyte membrane-fused Ce6-loaded liposomes. The resulting biomimetic nanoparticles were named B-Lip@PTX/Cur/Ce6. After intravenous administration, it is anticipated that B-Lip@PTX/Cur/Ce6 could evade macrophage uptake and immune system clearance, prolong circulation time in the bloodstream, and effectively accumulate at the tumor sites. Upon intracellular uptake, the photosensitizer Ce6 within the liposomal bilayer could generate $^1O_2$ when exposes to near-infrared light irradiation, thereby inducing a PDT effect on breast cancer. This process also triggers the sustained release of PTX and Cur within tumor cells, which counteracts MDR by inhibiting P-gp and enhances the efficacy of chemotherapy. The integration of photodynamic therapy, chemotherapy, and MDR inhibition into one biomimetic nanoplatform with controlled drug release promisingly overcomes the problems of premature drug release, development of MDR, and rapid blood clearance, thereby enabling more efficient breast cancer treatment.

Scheme 1. Illustration of the Biomimetic NDDS (B-Lip@PTX/Cur/Ce6)

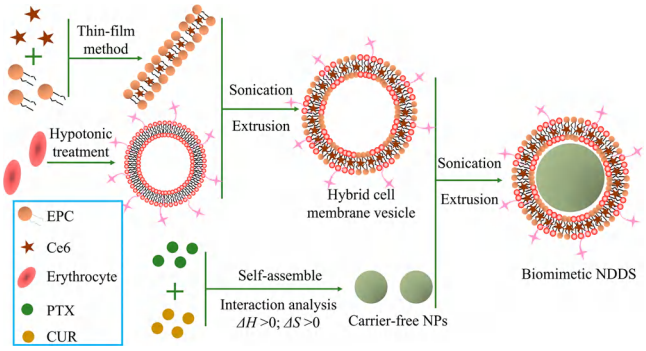

2. EXPERIMENTAL SECTION

2.1. Materials. Paclitaxel (PTX), chlorin e6 (Ce6), lecithin from egg (EPC), Me-β-CD (MβCD), cytochalasin D (CCD), cholesterol (Chol), singlet oxygen sensor green reagent (SOSG), and 2′,7′-dichlorodihydrofluorescein diacetate (DCFH-DA) were purchased from Dalian Meilun Biotechnology Co., Ltd. (Dalian, China). Curcumin (Cur) was provided by J&K Scientific Co., Ltd. (Beijing, China). Polyethylene glycol 2000-distearoylphosphatidylethanolamine ($DSPE\text{-}PEG_{2000}$) was purchased from Xi'an ruixi Biological Technology Co., Ltd. (Xi'an, China). Dulbecco's modified Eagle's medium (DMEM) with high glucose level, minimum Eagle medium (MEM), and Roswell Park Memorial Institute (RPMI)-1640 medium were obtained from Hyclone Thermo Scientific (Waltham, MA, USA). Penicillin and streptomycin were supplied by Gibco Thermo Scientific (Waltham, MA, USA). Fetal bovine serum (FBS) was procured from Excell Bio (Shanghai, China). 3-(4,5-Dmethylthiazol-2-yl)-2,5-diphenyltetrazolium bromide (MTT) was acquired from Sigma-Aldrich Chemicals (Germany). All other chemicals were commercially available

https://doi.org/10.1021/acsanm.4c02669
ACS Appl. Nano Mater. XXXX, XXX, XXX−XXX

as analytical-grade reagents and were used directly throughout the experiments without further purification.

2.2. Animals and Cell Lines. Mouse metastatic breast cancer cells (4T1) were cultured in RPMI 1640 medium containing 10% FBS, penicillin (100 U/mL), and streptomycin (100 μg/mL). Human breast cancer cells (MCF-7) were cultured in DMEM medium supplemented with 10% FBS, penicillin (100 U/mL), and streptomycin (100 μg/mL). Multidrug resistant human breast cancer cells (MCF-7/ADR) were cultured in MEM, in which 0.01 mg/mL insulin, 0.5−1 μg/mL adriamycin, 10% FBS, penicillin (100 U/mL), and streptomycin (100 μg/mL) were additionally added to maintain a drug resistant property. All cells were maintained in a humidified incubator (37 °C, 5% CO_2).

Female BALB/c mice (5−6 weeks, 20 ± 2 g) and female BALB/c nude mice (5−6 weeks, 20 ± 2 g) were purchased from Jinan Pengyue experimental animal breeding co. LTD (Jinan, China). The procedures for conducting animal experiments were granted approval by the Animal Ethics Committee of Liaocheng University and carried out in strict accordance with the guidelines and protocols of Ethical and Regulatory standards.

2.3. Interaction Investigation of PTX with Cur Molecules. Fluorescence spectra of PTX and Cur were acquired using a fluorescence spectrophotometer (F-7000, Hitachi, Japan). PTX and Cur were dissolved in DMSO of appropriate quantities. Twelve μM PTX was configured, and various concentrations of Cur (0, 12, 24, 36, 48, 60, 72, 84 μM) were added, respectively. The configured solutions were thoroughly mixed and allowed to reach equilibrium in a water bath at the corresponding temperature for a duration of 30 min. The fluorescence quenching spectra of PTX were recorded at disparate temperatures including 303.15, 308.15, and 313.15 K. The excitation wavelength was set at 409 nm, while the measurement wavelength range spanned from 350 to 650 nm. Both the excitation and emission slits were set at a width of 2.5 nm, and the scan rate was set at 1200 nm per minute.

2.4. Isolation of Erythrocyte Membrane (EM). Erythrocyte membrane (EM) was acquired through the process of hypotonic lysis. The whole blood was collected from the orbital vein of female BALB/c mice and stored in anticoagulation tubes, from which the red blood cells (RBCs) were subsequently obtained. RBCs were washed three times with 1× PBS (10 mM, pH 7.4) solution via centrifugation at a speed of 5 × 10^3 rpm for 5 min at 4 °C. Subsequently, the RBCs were lysed with 0.25 × PBS (2.5 mM, pH 7.4) in ice bath for a duration of 2 h. The resulting hemoglobin was carefully extracted and subjected to further centrifugation at 1 × 10^4 rpm for 15 min at 4 °C. The resulting pink pellet was collected and underwent multiple rounds of centrifugation at 3 × 10^3 rpm for 5 min at 4 °C, using 1× PBS as the washing solution, until the EM became colorless. The final EM was dispersed in 1× PBS solution and stored at −20 °C until subsequent use.

2.5. Preparation and Characterization of the Nanodrug Delivery System. PTX/Cur nanocrystals (PTX/Cur NCs) were prepared using an antisolvent precipitation method. In brief, a mixture of PTX and Cur at different molar ratios was dispersed in 3 mL of DMF and added dropwise into 15 mL of PBS (10 mM, pH 7.4) with sonication (100 W) in an ice bath. To eliminate DMF and unbound drugs, the resulting solution was transferred to a pretreated dialysis bag (MWCO, 8−14 kDa) and dialyzed with deionized water for 2 h under stirring, with the deionized water being changed every 30 min. The solution was then homogenized using a PhD D-3L homogenizer (PhD Technology LLC, Bloomington, MN, USA) for 5−10 min to reduce the particle size, resulting in the formation of PTX/Cur NCs.

Ce6-loaded liposomes were prepared using a modified thin film and hydration method.[32] Specifically, Ce6, EPC, Chol, and DSPE-PEG_{2000} (in a molar ratio of 3:60:20:2.8) were accurately weighed and dissolved in 5 mL of chloroform. The chloroform solution was then decompressed (−0.1 Pa) in a nightshade flask and evaporated to form a film, which was then hydrated with 5 mL of PBS (10 mM, pH 7.4). Subsequently, the Ce6-loaded liposomes were mixed and coextruded with the above EM through a series of polycarbonate membranes (800, 400, and 200 nm) for several cycles to form fusion liposomal bilayer vesicles, which were subjected to ultrasound with PTX/Cur NCs to obtain B-Lip@PTX/Cur/Ce6. The particle size of B-Lip@PTX/Cur/Ce6 was reduced using a D-3L homogenizer for another 10 min.

Particle size and zeta potential of PTX/Cur NCs and B-Lip@PTX/Cur/Ce6 were measured using the Malvern Zetasizer Nano ZSP dynamic light scattering (DLS) instrument (Malvern instruments, UK). The UV absorption and fluorescence spectra of Free drug (PTX, Cur, and Ce6 mixed solution, the same below) and B-Lip@PTX/Cur/Ce6 at the same drug concentrations were investigated using a U-3700 UV−vis spectrophotometer (Shimadzu, Japan) and fluorescence spectrophotometer (F-7000, Hitachi, Japan), respectively. The storage stability of B-Lip@PTX/Cur/Ce6 was evaluated by analyzing its particle size and zeta potential after being stored at 4 °C for 21 days. The morphology of PTX/Cur NCs, B-Lip@PTX/Cur/Ce6, and B-Lip@PTX/Cur/Ce6 after laser irradiation (650 nm, 500 mW/cm^2) for 1 h was observed with transmission electron microscopy (JEM-2100, JEOL, Japan). The content of PTX was determined via high-performance liquid chromatography (HPLC) with a C18 column (5 μm, 250 × 4.6 mm, Agilent) at 25 °C. The mobile phase (methanol:water = 70:30, v/v) was pumped at a flow rate of 1.0 mL/min, and the UV detector was set at 227 nm.

2.6. In Vitro Release Assay. A modified dialysis method was employed to evaluate the release of PTX from PTX/Cur NCs and B-Lip@PTX/Cur/Ce6 when subjected to laser irradiation. Specifically, a suspension of 2.0 mL PTX/Cur NCs or B-Lip@PTX/Cur/Ce6 at a PTX concentration of 100 μg/mL was sealed in dialysis bags (MWCO, 8−14 kDa), which were then placed within a conical flask containing 100 mL of PBS (10 mM, pH 7.4) with 1% (w/v) SDS. The experiments were conducted in a 37 °C water bath thermostatic shaker, with agitation at 150 rpm. Throughout the 72 h duration of the experiment, which necessitated strict light protection, the dialysis bags of the laser irradiation group were continuously exposed to a 650 nm laser (500 mW/cm^2). At regular intervals, 3.0 mL of the solution sample was collected from the external medium and replaced with an equal volume of fresh medium. HPLC analysis was used to calculate release profiles of PTX from different formulations. Data were reported as mean ± standard deviation (SD).

2.7. In Vitro Single-Linear Oxygen ($^1O_2$) Generation Assay. The measurement of single-linear oxygen ($^1O_2$) production by B-Lip@PTX/Cur/Ce6 under laser irradiation was conducted using a commercially available $^1O_2$ green fluorescent probe (Singlet oxygen sensor green reagent, SOSG). SOSG is a specific fluorescent probe utilized for the detection of $^1O_2$, which binds to $^1O_2$ and oxidizes, resulting in the production of SOSG-EP (oxidized SOSG) emitting green fluorescence. Initially, SOSG powder was dissolved in methanol to prepare an SOSG stock solution with a concentration of 5 mM. Subsequently, the SOSG stock solution was diluted to a final concentration of 2 μM with various preparations, including PBS, PTX/Cur NCs (25 μg/mL PTX and 5.5 μg/mL Cur), Free drug (25 μg/mL PTX, 5.5 μg/mL Cur, and 20 μg/mL Ce6), and B-Lip@PTX/Cur/Ce6 (25 μg/mL PTX, 5.5 μg/mL Cur, and 20 μg/mL Ce6), prior to being irradiated by a laser (650 nm, 500 mW/cm^2) for different times. The fluorescence intensity of SOSG-EP was then measured by an F-7000 fluorescence spectrophotometer (Hitachi, Japan) at the time points of 1, 3, 5, 10, 20, 30, and 60 min. Experimental conditions were set as follows: excitation wavelength 498 nm, emission wavelength 525.8 nm, temperature 298.2 K, excitation slit 5 nm, and emission slit 5 nm, respectively. All the above experiments were performed three times.

2.8. Intracellular Reactive Oxygen Species (ROS) Generation Detection. 2′,7′-Dichlorodihydrofluorescein diacetate (DCFH-DA), an intracellular reactive oxygen fluorescence probe, was utilized to assess the level of the produced ROS in 4T1 cells after treating with various formulations. Initially, 4T1 cells were seeded in 24-well plates at a density of 10^5 cells/well and incubated for 24 h with a medium containing PTX/Cur NCs (25 μg/mL PTX and 5.5 μg/mL Cur), Free drug (25 μg/mL PTX, 5.5 μg/mL Cur, and 20 μg/mL Ce6), and B-Lip@PTX/Cur/Ce6 (25 μg/mL PTX, 5.5 μg/mL Cur, and 20 μg/mL Ce6), respectively, followed by a 6 h incubation period. Ten μM of DCFH-DA dispersed in RPMI 1640 was then added into the cells, which were washed with PBS for 3 times in advance. The incubation of

https://doi.org/10.1021/acsanm.4c02669
ACS Appl. Nano Mater. XXXX, XXX, XXX−XXX

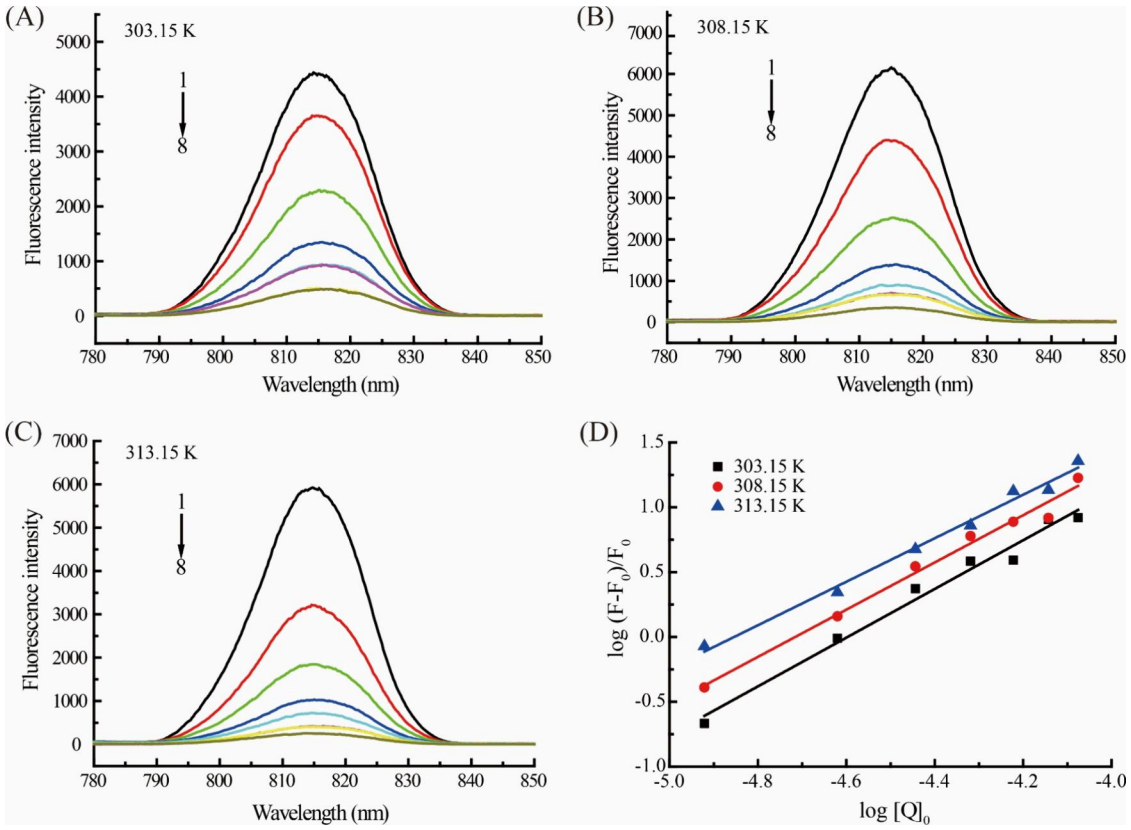

Figure 1. Fluorescence quenching spectra of PTX (12 μM) with different concentrations of Cur (1→ 8: 0−84 μM) at 303.15 K (A), 308.15 K (B), and 313.15 K (C), respectively. Double-logarithm plots for the fluorescence quenching of PTX by Cur (D).

the cells continued in the dark for 30 min. Subsequently, the cells were exposed to a NIR laser (650 nm, 500 mW/cm^2) for durations of 2, 5, and 10 min, respectively. The fluorescence emitted by DCF (the oxidation product of DCFH-DA in cells) in each group of cells was observed under a Nikon Eclipse Ti-s inverted fluorescence microscope (Nikon Ltd., Tokyo, Japan) to evaluate the intracellular ROS production.

2.9. Intracellular Uptake. To visualize the distribution of B-Lip@PTX/Cur/Ce6 in 4T1 cells, an inverted fluorescence microscope was employed to conduct cell uptake experiments. 4T1 cells were seeded in 24-well plates with 1 × 10^5 cells per well and incubated for 24 h. After that, fresh medium containing B-Lip@PTX/Cur/Ce6 solution (equivalent to 20 μg/mL Ce6) was replaced and incubated for varying durations of 0.5, 2, 4, 6, 8, and 24 h, with Free drug (equivalent to 20 μg/mL Ce6) utilized for comparison as well. The medium was then discarded, and the cells were washed thrice with PBS at pH 7.4. Subsequently, the cells were stained with Mito-Tracker Green FM (Sigma, St. Louis, Missouri, USA) at a concentration of 100 nM to visualize mitochondrial matrix and fixed using a 4% paraformaldehyde solution for a duration of 15 min, followed by three washes with PBS. The cells were then subjected to a 20 min staining process using Hoechst 33258 (Life Technologies, Carlsbad, CA), a nuclear dye with medium dilution. Finally, images capturing the intracellular accumulation of Ce6 and its distribution within subcellular organelles were acquired using a fluorescence microscope. Moreover, various experimental conditions were employed, including the utilization of cellular uptake inhibitors, such as methyl-β-cyclodextrin (MβCD), cytochalasin D (CCD), and sucrose, so as to identify the internalization pathway of B-Lip@PTX/Cur/Ce6 within the cells.

2.10. In Vitro Cytotoxicity Assay. The MTT method was applied for assessing the in vitro cytotoxicity of PTX formulations. Briefly, 4T1, MCF-7, and MCF-7/ADR cell suspensions were inoculated in 96-well plates at a density of 3 × 10^3 cells per well for a duration of 24 h. Following this, 100 μL of the previous cell medium was replaced with fresh medium containing varying concentrations of B-Lip@PTX/Cur/Ce6, PTX/Cur NCs, and Free drug. After a 4 h incubation period in the absence of light, some of the reagent sets underwent laser irradiation (650 nm, 500 mW/cm^2) for 5 min. Subsequently, the 96-well plates were further incubated in the dark for an additional 24 h. After a 4 h incubation period, 150 μL of dimethyl sulfoxide (DMSO) was added to each well, followed by 5 min of shaking to dissolve the formaldehyde crystals. The absorbance at 570 nm of each well was measured using a microplate reader (BioTek, USA). The half-inhibition concentration (IC_{50}) values and half-association index (CI_{50}) values were determined using GraphPad Prism version 5.0 (GraphPad, San Diego, CA, USA) and CompuSyn version 1.0 (CompuSyn, Paramus, NJ, USA), respectively.[9] The experiments were conducted in triplicate with five replicate wells per condition in each experiment.

2.11. Apoptosis. The apoptosis-inducing properties of B-Lip@PTX/Cur/Ce6+Laser, PTX/Cur NCs, and Free drug+Laser were further investigated using an Annexin V-FITC/PI apoptosis detection kit (Yeasen Biotechnology (Shanghai) Co., Ltd., Shanghai, China) according to the manufacturer's protocol. Briefly, 4T1 cells were seeded in a 6-well cell culture plate (5 × 10^5 cells per well) and incubated for 12 h. B-Lip@PTX/Cur/Ce6, PTX/Cur NCs, and Free drug at a PTX concentration of 10 μg/mL were added into the cells. After a 4 h incubation period in the absence of light, B-Lip@PTX/Cur/Ce6 and Free drug underwent laser irradiation (650 nm, 500 mW/cm^2) for 5 min. After incubation for another 8 h, the cells were harvested with trypsinization without EDTA and washed twice with PBS. Subsequently, the samples were stained with Annexin V-FITC and PI and tested by flow cytometry (CytoFLEX, Beckman Coulter).

2.12. In Vivo Antitumor Efficacy Study. In order to establish a mouse tumor transplantation model and assess the in vivo antitumor effectiveness of various preparations, female BALB/c mice were subcutaneously inoculated with 1 × 10^6 4T1 cells. Once the tumors reached approximately 50−80 mm^3 in size, the 4T1 tumor-bearing mice were randomly assigned to six groups as follows: (1) saline as the control group, (2) Free drug (PTX 5.0 mg/kg, Cur 1.1 mg/kg, Ce6 4 mg/kg), (3) Free drug+Laser, (4) PTX/Cur NCs (PTX 5.0 mg/kg,

https://doi.org/10.1021/acsanm.4c02669
ACS Appl. Nano Mater. XXXX, XXX, XXX−XXX

Cur 1.1 mg/kg), (5) B-Lip@PTX/Cur/Ce6 (PTX 5.0 mg/kg, Cur 1.1 mg/kg, Ce6 4 mg/kg, and (6) B-Lip@PTX/Cur/Ce6+Laser. Each group contained six mice, which received a 0.2 mL injection every 2 days, with the Laser treatment group additionally receiving 10 min of laser irradiation (650 nm, 500 mW/cm^2) after 4 h of drug administration. The body weight of the mice was monitored daily, and their relative body weight was calculated according to the following formula: relative body weight = mice weight at day$_n$/mice weight at day$_0$. The daily recording of tumor volume was conducted as well and calculated using the following formula: tumor volume= (length × width^2)/2. Following a period of 14 days, the mice were euthanized through cervical dislocation, and the major organs including the heart, liver, spleen, lung, kidney, and tumor tissues were promptly extracted. Hematoxylin-eosin (H&E) staining and terminal-deoxynucleotidyl transferase mediated dUTP nick end labeling (TUNEL) assays were subsequently employed to assess the antitumor efficacy and biosafety of each formulation. In order to further elucidate the biosafety of each group, the measurement of aspartate transaminase (AST), alanine transaminase (ALT), urea nitrogen (BUN), and creatinine (CRE) values in each group of mice was carried out using the respective kits (Nanjing Jiancheng Bioengineering Institute, Nanjing, China) following the manufacturer's instructions.

2.13. Immunohistochemical Assay. An immunohistochemical assay was applied to detect the expression of IL-6, TNF-α, P-gp, and CD8 in tumor tissues of 4T1 tumor-bearing mice treated with B-Lip@PTX/Cur/Ce6+Laser, Free drug+Laser, PTX/Cur NCs, and saline. The tumor tissues were formalin-fixed, paraffin-embedded, and cut with a microtome (5 μm sections). Then, sections were deparaffinized, hydrated, and incubated with primary antibodies (Servicebio, China), respectively, overnight at 4 °C. Subsequently, sections were further treated with secondary antibody (Servicebio, China) for 50 min at room temperature, visualized with 3,3′-diaminobenzidine (DAB) (Servicebio, China), and counterstained using hematoxylin. After that, the expression of proteins was visualized with a Nikon Eclipse Ti-s inverted fluorescence microscope (Nikon Ltd., Tokyo, Japan). Data were given based on five random visual fields.

2.14. In Vivo and Ex Vivo Imaging. Subcutaneous inoculation of 4T1 cells (5 × 10^6 cells/mL) was performed in the right axilla of 10 female mice, which were evenly divided into two groups. Once the tumor volume reached approximately 80−100 mm^3, 200 μL of either Free drug or B-Lip@PTX/Cur/Ce6 (both at a dose of 5 mg/kg Ce6) was injected into the tail vein. Mice were subsequently imaged at various time intervals (0.5, 1, 2, 4, 8, 12, and 24 h) using a Lumina III system (PerkinElmer, Waltham, MA, USA). After 24 h of administration, tumors and major organs, including heart, liver, spleen, lung, and kidney, were excised for ex vivo imaging under identical conditions.

2.15. Statistical Analysis. The experiments were repeated a minimum of three times, and the resulting data were recorded as the mean value plus or minus the standard deviation (SD). Statistical analysis was performed using the Student t test for independent samples and one-way ANOVA with SPSS 19.0 software. A significance level of $p < 0.05$ was considered statistically significant, while a significance level of $p < 0.01$ was considered highly significant.

3. RESULTS AND DISCUSSION

3.1. Self-Assembly Mechanism of PTX and Cur. Fluorescence spectroscopy is a commonly employed technique for chemical thermodynamic investigations, and the fluorescence burst spectra of PTX (12 μM) with different concentrations of Cur at various temperatures are plotted in Figures 1A−C. Obviously, the fluorescence intensity of PTX diminished gradually with the increase of the Cur concentrations, whereas the emission peak remained relatively unchanged. The widely utilized Stern−Volmer equation[33] as follows was applied to elucidate the quenching mechanism of the system

$$\frac{F}{F_0} = 1 + K_{sv}[Q]_0 = 1 + k_q\tau_0[Q]_0 \quad (1)$$

where F_0 and F represent the fluorescence intensities of PTX in the absence and presence of Cur, respectively. $[Q]_0$ is the concentration of the burster Cur. τ_0 is the average fluorescence lifetime of the fluorescent molecule PTX in the absence of the burster Cur, usually about 10^{-8} s. K_{sv} is the Stern−Volmer burst constant, and k_q is the burst rate constant for the burst reaction.

The values of K_{sv} and k_q were determined by plotting F_0/F against $[Q]_0$. Given that the value of k_q exceeded 2.0×10^{10} M^{-1} s^{-1} (Table S1), which was the maximum dynamic burst constant, the burst mechanism of the system should be classified as a static burst.[34] The determination of the number of binding sites (n) and binding constants (K_a) (Figure 1D and Table S1) for PTX to Cur was also accomplished via the equation[35]

$$\log\left[\frac{(F_0 - F)}{F}\right] = \log K_a + n \log[Q]_0 \quad (2)$$

where F_0 and F represent the fluorescence intensities of PTX in the absence and presence of Cur, respectively. $[Q]_0$ is the concentration of the burster Cur, n is the number of binding sites, and K_a is the binding constant.

The n values, approximately 2.0, indicated that there were binding affinities between PTX and Cur at approximately two binding sites. Furthermore, K_a values above 10^5 indicated a strong binding affinity among the binary system. The K_a values exhibited an upward trend as the temperature rose, implying that the binding interaction between PTX and Cur should be in a heat-absorbing manner.[36]

To gain a deeper understanding for the binding process of PTX/Cur, the Gibbs free energy change (ΔG), enthalpy change (ΔH), and entropy change (ΔS) were calculated through a van't Hoff analysis.[37]

$$\Delta G^\circ = \Delta H^\circ - T\Delta S^\circ = -RT \ln K_a \quad (3)$$

The corresponding thermodynamic data can be found in Table S1. Negative ΔG values, positive ΔH values, and positive ΔS values collectively indicated that the binding process was generally driven by entropy and hydrophobic interactions were crucial in the binding process.

3.2. Fabrication of B-Lip@PTX/Cur/Ce6. The optimal molar ratio for the combination of PTX with Cur was further verified through an MTT assay prior to the preparation of B-Lip@PTX/Cur/Ce6. Specifically, 4T1 cells were exposed to various molar ratios of PTX/Cur, and the resulting combination index (CI_{50}) was calculated and recorded in Table S2. CI_{50} values greater than 1, equal to 1, and less than 1 indicate antagonistic, allelopathic, and synergistic effects of the combined drugs, respectively.[38] The lowest CI_{50} values were observed when the molar ratio of PTX to Cur was 2:1, indicating the most efficient inhibition of 4T1 cell growth. Furthermore, PTX/Cur NCs were prepared with different PTX/Cur molar ratios. As shown in Table S3, PTX/Cur NCs at a PTX/Cur molar ratio of 2:1 (homogenized for 5 min) exhibited the smallest particle size and the lowest IC_{50} value. Accordingly, the optimal molar ratio of PTX to Cur for subsequent experiments was determined as 2:1 (mol:mol).

B-Lip@PTX/Cur/Ce6 was successfully prepared by applying a two-step process involving the fabrication of the carrier-free PTX/Cur NCs, followed by the coating of the fusion liposomal bilayer vesicles composed of EM and Ce6-loaded liposomes on

https://doi.org/10.1021/acsanm.4c02669
ACS Appl. Nano Mater. XXXX, XXX, XXX−XXX

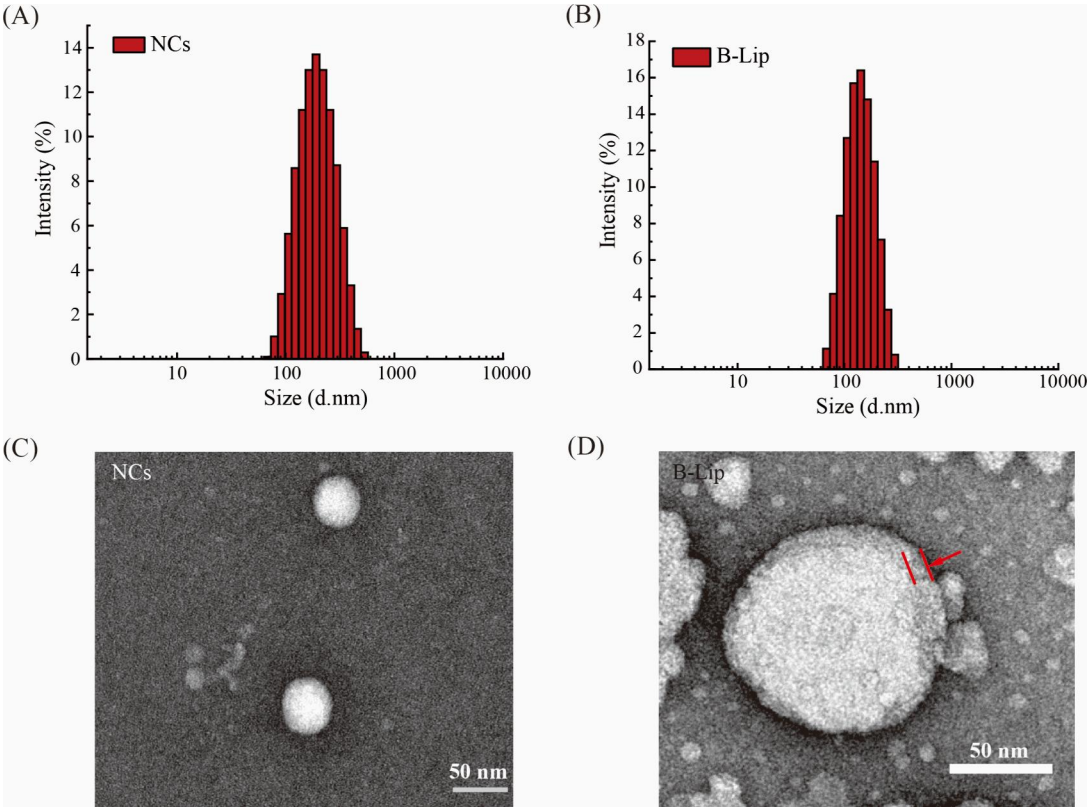

Figure 2. Particle size distribution of PTX/Cur NCs (NCs) (A) and B-Lip@PTX/Cur/Ce6 (B-Lip) (B) determined by DLS results. TEM images of PTX/Cur NCs (NCs) (C) and B-Lip@PTX/Cur/Ce6 (B-Lip) (D).

their surface. To confirm the successful transfer of EM to B-Lip@PTX/Cur/Ce6, the retention of EM proteins on B-Lip@PTX/Cur/Ce6 was identified by SDS-polyacrylamide gel electrophoresis (SDS-PAGE). As depicted in Figure S1, the results of SDS-PAGE demonstrated a close resemblance between the protein bands of B-Lip@PTX/Cur/Ce6 and the EM, as observed through brilliant Coomassie blue staining, verifying the successful transfer of membrane proteins to the surface of B-Lip@PTX/Cur/Ce6. Thus, carrier-free PTX/Cur NCs were proved to be effectively wrapped by the biomimetic fusion liposomal bilayer vesicles. To further ensure the successful loading of PTX, Ce6, and Cur, the UV−vis absorbance spectra of Free drug and B-Lip@PTX/Cur/Ce6 were measured as well. As seen in Figure S2A, the absorption peaks of Cur and Ce6 in the spectrum of B-Lip@PTX/Cur/Ce6 were displaced slightly from the spectrum of the Free drug at an equivalent drug concentration, indicating that the environment around the drugs was altered. Besides, fluorescence spectroscopy is an effective way to investigate the structural and conformational changes of the system. Changes in fluorescence intensity or emission maximum are utilized to study the binding mechanisms of the drugs. As shown in Figure S2B, the fluorescence intensities of PTX, Cur, and Ce6 were significantly quenched or boosted in comparison with Free drug at equivalent drug concentrations, which also indicated the structural and conformational changes of the environment around the drugs.[39]

3.3. Characterization and Stability of B-Lip@PTX/Cur/Ce6. B-Lip@PTX/Cur/Ce6 revealed a hydrodynamic particle size of 135.8 ± 2.9 nm and a polydispersity index of 0.267 ± 0.012 (Figure 2B), which is considered favorable for their efficient accumulation in tumor tissues via passive targeting. Besides, PTX/Cur NCs exhibited a hydrodynamic particle size distribution of 232.5 ± 4.4 nm with a relatively narrow particle size distribution (PDI = 0.185 ± 0.010) (Figure 2A).

Additionally, as shown in Figure 2C, PTX/Cur NCs exhibited a uniform size and spherical shape in their TEM images, with an average particle size of approximately 50 nm. In contrast, B-Lip@PTX/Cur/Ce6 possessed an elliptical shape with a particle size of 80 nm and exhibited a distinct core−shell structure morphology (indicated by an arrow in Figure 2D), implying the successful fabrication of B-Lip@PTX/Cur/Ce6. It is noteworthy that the dehydration and wrinkling of B-Lip@PTX/Cur/Ce6 and PTX/Cur NCs during the TEM sample preparation resulted in slightly smaller particle sizes observed in their TEM photographs compared to the values acquired by DLS.[15]

The stability tests of B-Lip@PTX/Cur/Ce6 were conducted during a test period of 21 days. Throughout the storage period, the maximum particle size of B-Lip@PTX/Cur/Ce6 was 182.3 ± 2.5 nm, which slightly surpassed the average particle size, yet remained within the lower nanometer range, revealing that no significant alteration in particle size was observed (Figure S3A). Furthermore, the mean value of the ζ-potential exhibited minor fluctuations over time, but these fluctuations were not statistically significant compared to the initial value on day_0 (Figure S3B). These findings provided evidence of the stability of B-Lip@PTX/Cur/Ce6, verifying that the fabrication strategy of the nanoparticles with a core−shell structure was tremendously successful.

3.4. Laser-Triggered In Vitro Release of PTX. The enhancement of liposomal bilayer shell permeation can be achieved through oxidative stress under photodynamic reactions. Thus, the drug release characteristics of B-Lip@PTX/Cur/Ce6, which was laser responsive, were investigated in

https://doi.org/10.1021/acsanm.4c02669
ACS Appl. Nano Mater. XXXX, XXX, XXX−XXX

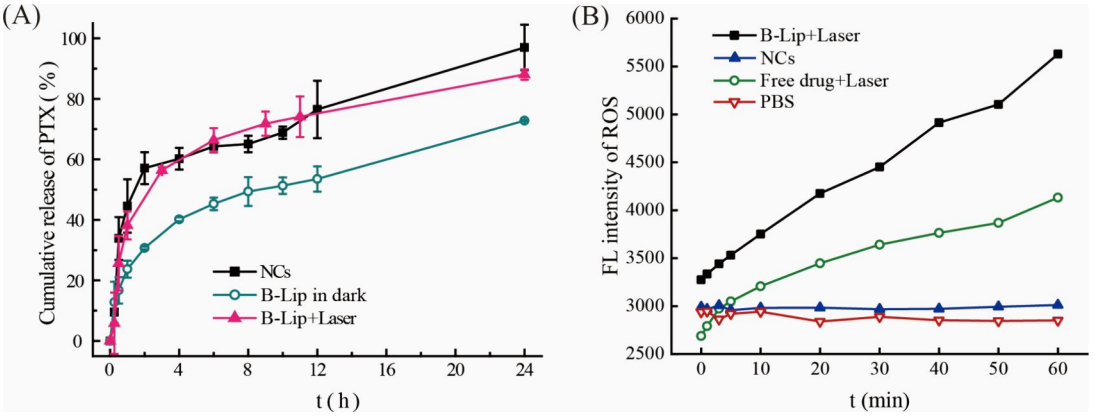

Figure 3. Cumulative release profiles of PTX from PTX/Cur NCs (NCs) and B-Lip@PTX/Cur/Ce6 (B-Lip) with or without laser irradiation in 0.1 M PBS (pH 7.4) involving 1% (w/v) SDS (n = 3) (A). Singlet oxygen formation of PBS, PTX/Cur NCs (NCs), Free drug (PTX, Cur, and Ce6 mixed solution)+Laser, and B-Lip@PTX/Cur/Ce6 (B-Lip)+Laser measured by an SOSG probe in vitro (B).

comparison with PTX/Cur NCs. As shown in Figure 3A, the cumulative released amount of PTX from PTX/Cur NCs initially exhibited a rapidly increasing trend, reaching approximately 60% within a 2 h period. However, the release rate of PTX/Cur NCs slowed down during the subsequent 22 h and eventually approached nearly 100% release at approximately 24 h. Significantly, the release profile of PTX in B-Lip@PTX/Cur/Ce6 upon laser irradiation exhibited similarity to that of PTX/Cur NCs and demonstrated a notable increase when compared to B-Lip@PTX/Cur/Ce6 in the absence of a laser. Besides, the release of B-Lip@PTX/Cur/Ce6 was also verified via TEM, as the TEM image of B-Lip@PTX/Cur/Ce6 after laser-triggered release (Figure S4C) showed an apparently different morphology compared to normal B-Lip@PTX/Cur/Ce6 (Figure S4B). This phenomenon implied that the accelerated release of PTX from B-Lip@PTX/Cur/Ce6 could be primarily attributed to the lipid peroxidation of the fusion liposomal membranes surrounding the PTX/Cur NCs core, which arose from the ROS produced by the photosensitizer agents under laser irradiation.[15] The laser-triggered release profiles of B-Lip@PTX/Cur/Ce6 confirmed its laser-responsiveness for exerting selective cytotoxicity in tumor tissues and simultaneously reducing its side effects.

3.5. Detection of In Vitro Singlet Oxygen ($^1O_2$). The capability of B-Lip@PTX/Cur/Ce6 to generate singlet oxygen ($^1O_2$) in vitro under 650 nm laser irradiation was analyzed with singlet oxygen sensor green (SOSG). It is clear that the fluorescence intensities of SOSG-EP (oxidized SOSG) in the B-Lip@PTX/Cur/Ce6+Laser group and Free drug+Laser group were enhanced remarkably (Figure 3B), indicating the production of ROS induced by laser irradiation. Conversely, there were minimal fluctuations in the fluorescence intensity of PBS and PTX/Cur NCs, whose $^1O_2$ generation was negligible. Besides, at equivalent Ce6 concentrations and irradiation time, B-Lip@PTX/Cur/Ce6 exhibited a significantly higher production of $^1O_2$ compared to Free drug, further indicating the exceptional $^1O_2$-generating capability of B-Lip@PTX/Cur/Ce6. The generation of $^1O_2$ exhibited a positive correlation with the duration of laser irradiation, albeit to a moderate extent. These findings indicated that under laser irradiation, B-Lip@PTX/Cur/Ce6 could efficiently generate ROS and enhance the efficiency of photodynamic therapy.

3.6. Singlet Oxygen ($^1O_2$) Determination of B-Lip@PTX/Cur/Ce6 within 4T1 Cells. The photodynamic properties of various preparations in 4T1 cells were confirmed through the utilization of 2,7-dichlorofluorescein diacetate (DCFH-DA). Following hydrolysis of DCFH-DA by esterases within 4T1 cells, the resulting product undergoes oxidation by ROS, leading to the formation of fluorescent DCF. As shown in Figure 4A, basically no fluorescence was detected in cells treated with both

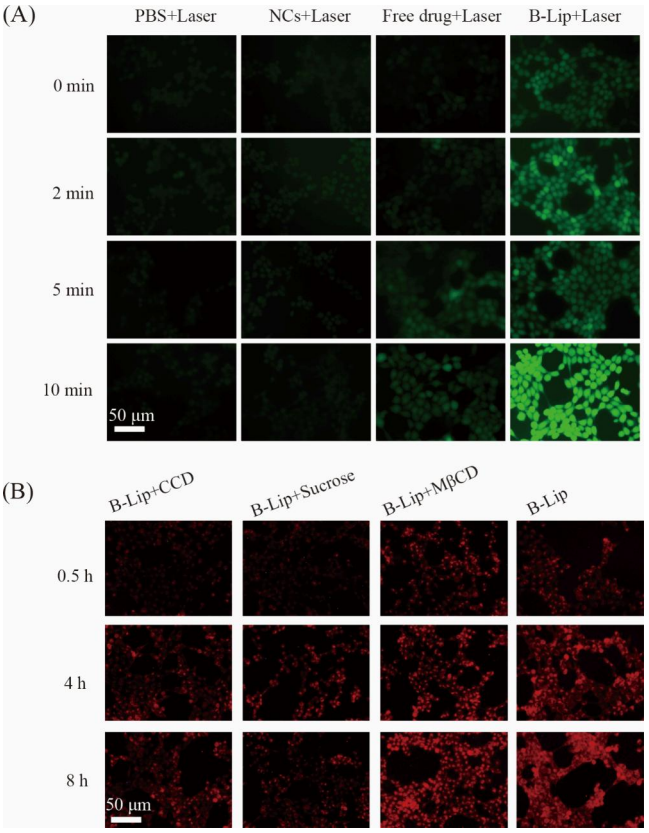

Figure 4. (A) Representative fluorescence microscopy images of intracellular singlet oxygen generated by DCFH-DA in 4T1 cells incubated with different formulations at different laser irradiation times: scale bar, 50 μm; NCs, PTX/Cur NCs; Free drug: PTX, Cur, and Ce6 mixed solution; B-Lip, B-Lip@PTX/Cur/Ce6. (B) Representative fluorescence microscopy images of 4T1 cells incubated with B-Lip@PTX/Cur/Ce6 (B-Lip) plus different inhibitors for different incubated times: scale bar, 50 μm.

https://doi.org/10.1021/acsanm.4c02669
ACS Appl. Nano Mater. XXXX, XXX, XXX−XXX

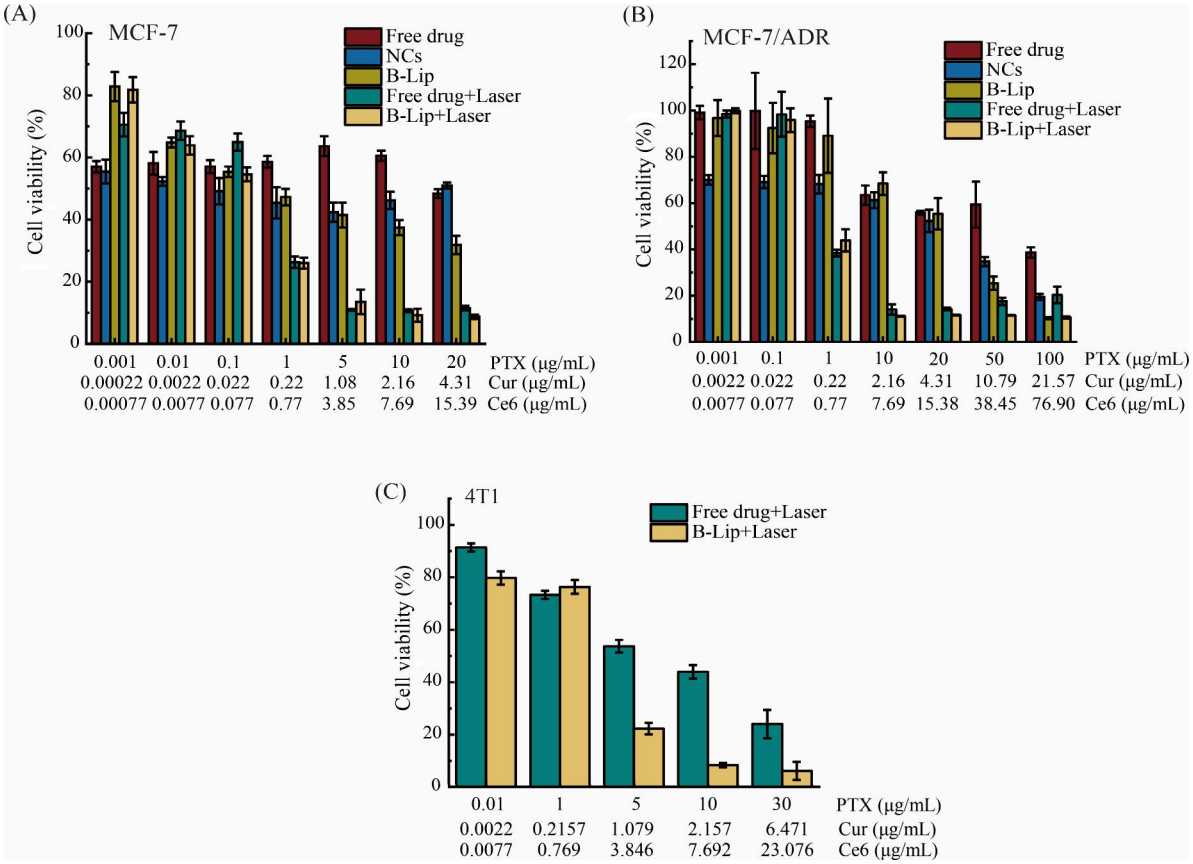

Figure 5. In vitro cell viability of MCF-7 cells (A), MCF-7/ADR cells (B), and 4T1 cells (C) after incubation with various formulations with or without laser irradiation (λ = 650 nm, 500 mW, 5 min): Free drug, PTX, Cur, and Ce6 mixed solution; NCs, PTX/Cur NCs; B-Lip, B-Lip@PTX/Cur/Ce6.

PBS and PTX/Cur NCs groups, while the fluorescence signal of Free drug exhibited slight enhancement following 10 min of laser irradiation. Conversely, cells treated with B-Lip@PTX/Cur/Ce6 demonstrated an significantly enhanced fluorescence signal after laser irradiation, accompanied by the observation of the correlation between the increase of fluorescence intensity and irradiation duration, verifying that B-Lip@PTX/Cur/Ce6 was responsible for a significant production of intracellular ROS.

3.7. Cellular Uptake. The cellular uptake mechanism investigation of nanodrug delivery systems holds significant importance in comprehending the pathways through which these systems are internalized by cells. The visualization of the cellular uptake paths of B-Lip@PTX/Cur/Ce6 was conducted via an inverted fluorescence microscope in this study (Figure 4B). The application of cellular uptake inhibitor cytochalasin D (CCD) and sucrose, which inhibited the macropinocytosis and clathrin-mediated endocytosis pathway, respectively, resulted in a substantial decrease in the fluorescence intensity of the formulation. In contrast, the addition of Me-β-CD (MβCD), a caveolae-mediated endocytosis inhibitor, did not have a significant impact on the fluorescence intensity of B-Lip@PTX/Cur/Ce6 compared to the normal group absent of cellular uptake inhibitor. These findings provided confirmation that the primary cellular uptake pathways for B-Lip@PTX/Cur/Ce6 were macropinocytosis and the clathrin-mediated endocytosis pathway.

Figure S5 demonstrates that 4T1 cells subjected to an 8 h incubation with B-Lip@PTX/Cur/Ce6 displayed significantly enhanced red fluorescence, whereas relatively slight red fluorescence was detected within the cells incubated for 0.5 h, indicating a clear temporal correlation for the uptake of B-Lip@PTX/Cur/Ce6 into 4T1 cells. Besides, the gradual increase in the red fluorescence signal detected in 4T1 cells following prolonged incubation with B-Lip@PTX/Cur/Ce6 could be attributed to the cytoplasmic enrichment of the nanoparticles through cellular endocytosis. Furthermore, to investigate the subcellular distribution of B-Lip@PTX/Cur/Ce6, Hoechst 33258 and Mito Tracker Green FM were utilized to label the nucleus and mitochondria of the cells, respectively. The red fluorescence emitted by B-Lip@PTX/Cur/Ce6 predominantly overlapped with the green fluorescence emitted by Mito-Tracker Green FM, resulting in a yellow appearance in the merged view and indicating that the internalization of B-Lip@PTX/Cur/Ce6 into cells was primarily localized within the mitochondria. It is worth noting that P-gp functions as an ATP-dependent efflux pump, while mitochondria serve as the primary source of ATP generation.[40] Thus, the increased uptake of B-Lip@PTX/Cur/Ce6 into tumor cells might result in reduced efflux.

Generally, the aforementioned study demonstrated the rapid and continuous uptake of B-Lip@PTX/Cur/Ce6 into 4T1 cells, resulting in significant cytoplasmic accumulation and longer time of drug accumulation in cells in contrast to Free drug (Figure S6). The cellular uptake of B-Lip@PTX/Cur/Ce6 facilitated transmembrane drug transport and served as the basis for the antitumor multidrug resistance effect of chemo-photodynamic combination therapy.

3.8. In Vitro Anticancer Activity. The primary mechanism of MDR in cancer cells is believed to be the overexpression of the membrane drug efflux pump (P-gp). Functioning as an ATP-

https://doi.org/10.1021/acsanm.4c02669
ACS Appl. Nano Mater. XXXX, XXX, XXX−XXX

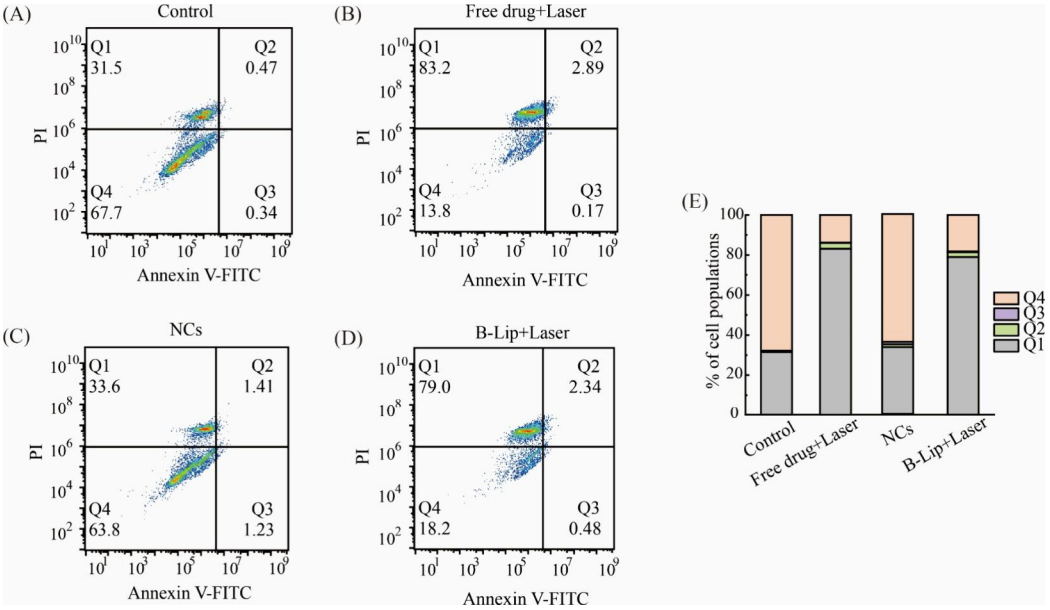

Figure 6. Quantification of apoptosis in 4T1 cells using an annexin V-FITC/PI staining assay: (A) blank control; (B) Free drug (PTX, Cur, and Ce6 mixed solution)+Laser; (C) PTX/Cur NCs (NCs); (D) B-Lip@PTX/Cur/Ce6 (B-Lip)+Laser; (E) the stacking columns (Q1, necrotic/dead cells; Q2, late apoptotic cells; Q3, early apoptotic cells; Q4, intact cells).

binding cassette transporter, P-gp actively transports multiple drugs out of cells, resulting in a reduction of intracellular drug concentrations below the lethal threshold. To address the question at hand, the introduction of a P-gp inhibitor such as Cur into the nano delivery system was necessary to enhance the chemosensitivity of MCF-7/ADR cells to PTX resistance. As shown in Table S4, it was evident that MCF-7/ADR cells exhibited a substantial level of drug resistance toward PTX molecules due to the unacquired IC_{50} value. The inclusion of the P-gp inhibitor Cur in PTX/Cur NCs resulted in lower IC_{50} values compared to free PTX alone, indicating the potential of Cur to effectively reverse MDR, as previously reported.[41] Additionally, B-Lip@PTX/Cur/Ce6+Laser showed superior cytotoxicity against all three cell lines (Figure 5 and Table S3), suggesting that the combined chemo-PDT and MDR reversal agents could combat drug resistance and was an attractive therapeutic strategy for anticancer.

3.9. Apoptosis Assay. An apoptosis assay was further applied to investigate the cytotoxicity mechanism among control, PTX/Cur NCs, Free drug+Laser, and B-Lip@PTX/Cur/Ce6+Laser groups (Figure 6). Quadrants shortened with "Q" (Q1, Q2, Q3, and Q4) were used to calculate quadrant proportions in order to calculate apoptotic and necrotic cell percentages.[42] Apparently, Free drug+Laser and B-Lip@PTX/Cur/Ce6+Laser induced maximum apoptosis and necrosis cell percentages of 86.26% and 81.82% (Q1 + Q2 + Q3), respectively. Meanwhile, the apoptosis and necrosis cell percentages induced by both the control group and PTX/Cur NCs were insignificant (32.31% and 36.24%, respectively). This phenomenon was in good accordance with the cytotoxicity assay, in which both Free drug+Laser and B-Lip@PTX/Cur/Ce6+Laser exhibited significant cytotoxicity in comparison with PTX/Cur NCs, verifying the effectiveness of the combined chemo-PDT therapeutic strategy for cancer treatment.

3.10. In Vivo Antitumor Effect. A 4T1 tumor-bearing mice model was applied in order to investigate the combined multidrug and multitreatment antitumor therapeutic efficacy of B-Lip@PTX/Cur/Ce6. The changes in tumor volume observed in mice following treatment with various agents are illustrated in Figure 7A. The tumor volume of the B-Lip@PTX/Cur/Ce6+Laser group was significantly lower than those for the other groups. At the end of the experiment, the ultimate tumor weight of the mice in the B-Lip@PTX/Cur/Ce6+Laser group also exhibited a statistically significant reduction compared to the other five groups ($p < 0.005$) (Figure 7C). Notably, the B-Lip@PTX/Cur/Ce6+Laser group displayed the most efficient inhibition of tumor growth, with a rate of 61.78% (Figure 7D). The remarkably improved therapeutic efficacy observed in B-Lip@PTX/Cur/Ce6+Laser treatment could probably be attributed to the utilization of EM encapsulation, which facilitates nanoparticle accumulation within tumors. In addition, the inhibitory effect of Cur on P-gp reduced the likelihood of PTX efflux, leading to a robust synergistic effect of the combined chemo-photodynamic therapy. Therefore, the administration of a synergistic dose of B-Lip@PTX/Cur/Ce6+Laser effectively enhanced the therapeutic effectiveness against tumors. Besides, by the end of the trial, the tumor inhibition rates of PTX/Cur NCs and B-Lip@PTX/Cur/Ce6 groups were 28.68% and 27.65%, respectively. The Free drug group demonstrated lower relative effectiveness in comparison to the saline group, with a tumor inhibition rate of approximately 17.10%. Interestingly, the Free drug+Laser group demonstrated superior tumor growth inhibition (42.81%), indicating the promising therapeutic potential of photodynamic therapy (PDT) in treating tumors.

Histological analysis using H&E staining (Figure 7E) revealed the presence of necrotic cells and evident cellular necrosis in tumors for the B-Lip@PTX/Cur/Ce6+Laser-treated group, confirming the combined efficacy of PDT and chemotherapy at the cellular level. Additionally, TUNEL experiments demonstrated that B-Lip@PTX/Cur/Ce6+Laser treatment induced widespread tumor apoptosis, characterized by the presence of shrunken nuclei, fragmented nuclei, and morphological pleomorphism. These findings aligned well with the treatment outcomes observed in the H&E-stained images.

Furthermore, the assessment of biosafety was extended by examining weight variations, conducting histological analysis on

https://doi.org/10.1021/acsanm.4c02669
ACS Appl. Nano Mater. XXXX, XXX, XXX−XXX

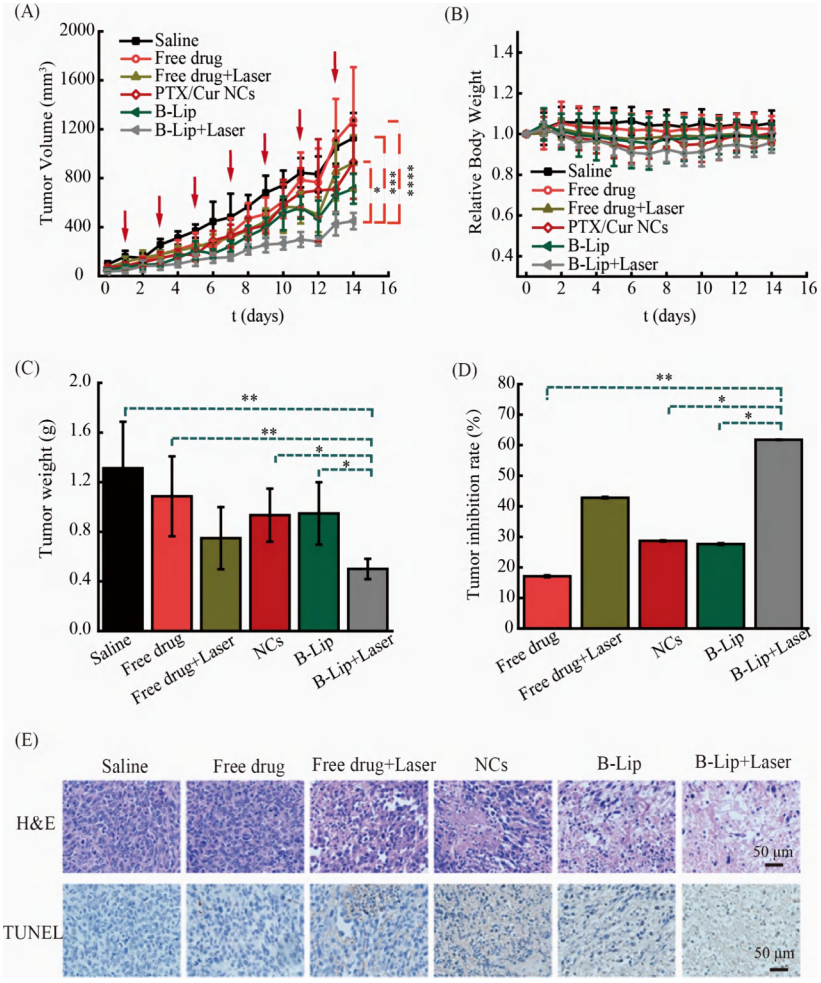

Figure 7. In vivo antitumor efficacy of different formulations by the intravenous route: tumor volume changes (A), body weight changes (B), tumor weight (C), and tumor inhibition rate (D) of 4T1-bearing BALB/c mice after treatment with different formulations. For each animal, seven consecutive doses were given (marked by arrows). Data represent mean ± SD ($n = 6$). (E) Representative H&E and TUNEL-positive (brown-stained) cells of tumor tissues from mice treated with different formulations: red arrow, single drug administration; Free drug, PTX, Cur, and Ce6 mixed solution; NCs, PTX/Cur NCs; B-Lip, B-Lip@PTX/Cur/Ce6.

vital organs, and assessing the plasma biochemical index. As shown in Figure 7B, no substantial weight loss occurred in any of the groups during treatment ($p > 0.05$), indicating that systemic toxicity was absent. Notably, no discernible abnormalities in major organs, including the heart, liver, spleen, lungs, and kidneys, were observed following all the formulation treatments, as evidenced by H&E staining (Figure S7). Moreover, the analysis of serum biochemical values pertaining to kidney and liver function revealed no significant deviations from the control group (Table S5), indicating the minimal occurrence of adverse effects associated with all the treated groups. Therefore, B-Lip@PTX/Cur/Ce6 exhibited promising potential for cancer therapy, owing to its excellent biocompatibility and effective inhibition of tumor growth.

3.11. Inflammation Inhibition and Immune Activation. Chronic inflammation plays a vital role in promoting tumor proliferation, matrix degradation, and immunosuppression, which is consequently tightly associated with tumor occurrence, invasion, and metastasis. IL-6 and TNF-α display central roles in promoting inflammation and metastasis in the tumor microenvironment (TME).[43] Thus, the expression of IL-6 and TNF-α in 4T1 tumor tissues in vivo was measured by immunohistochemistry. As shown in Figure 8, the inflammation inhibitory properties of B-Lip@PTX/Cur/Ce6 (B-Lip)+Laser were confirmed, as their micrographs of IL-6 showed obvious downregulation in comparison with PTX/Cur NCs ($P < 0.05$) and Saline ($P < 0.001$). Significantly decreased expression of TNF-α was also observed in B-Lip@PTX/Cur/Ce6 (B-Lip)+Laser in contrast to Free drug+Laser ($P < 0.05$) and Saline ($P < 0.001$). In summary, B-Lip@PTX/Cur/Ce6 showed great potential in reducing tumor-related inflammation through the suppression of IL-6 and TNF-α.

PTX induces overexpression of P-gp in tumor cells, which confers resistance of recurrent tumors to various anticancer drugs.[44] Thus, immunohistochemical staining was also used to analyze the expression of P-gp (Figure 9A). B-Lip@PTX/Cur/Ce6+Laser significantly downregulated the expression of P-gp protein levels compared to Free drug+Laser ($P < 0.05$) and Saline groups ($P < 0.001$), indicating that B-Lip@PTX/Cur/Ce6 had significant activity in reversing MDR (Figure 9C), which holds promise for treating MDR in ABC by combination of the chemotherapeutic drug PTX with the P-gp inhibitor Cur. Notably, PTX/Cur NCs also exhibited obviously decreased expression of P-gp attributed to their efficient internalization by cells. Besides, the suppressed immune responses in tumors play an essential role in promoting immune evasion and metastasis of

https://doi.org/10.1021/acsanm.4c02669
ACS Appl. Nano Mater. XXXX, XXX, XXX−XXX

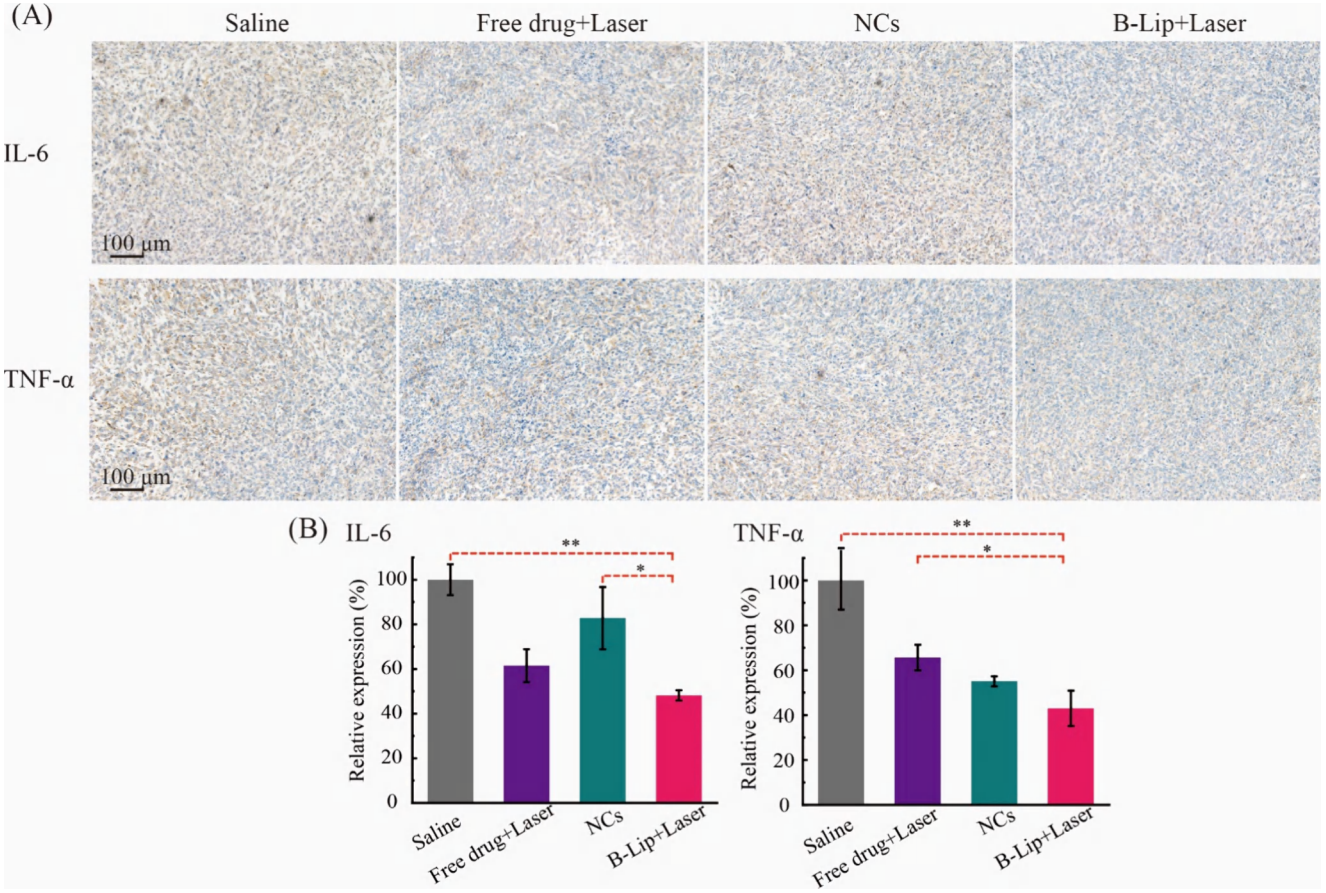

Figure 8. IL-6 and TNF-α in the tumor tissues of the Saline, Free drug (PTX, Cur, and Ce6 mixed solution)+Laser, PTX/Cur NCs (NCs), and B-Lip@PTX/Cur/Ce6 (B-Lip)+Laser groups in an antitumor detection assay in vivo tested by immunohistochemistry: (A) representative micrographs; (B) quantified data. $^{**}P < 0.001$ and $^{*}P < 0.05$.

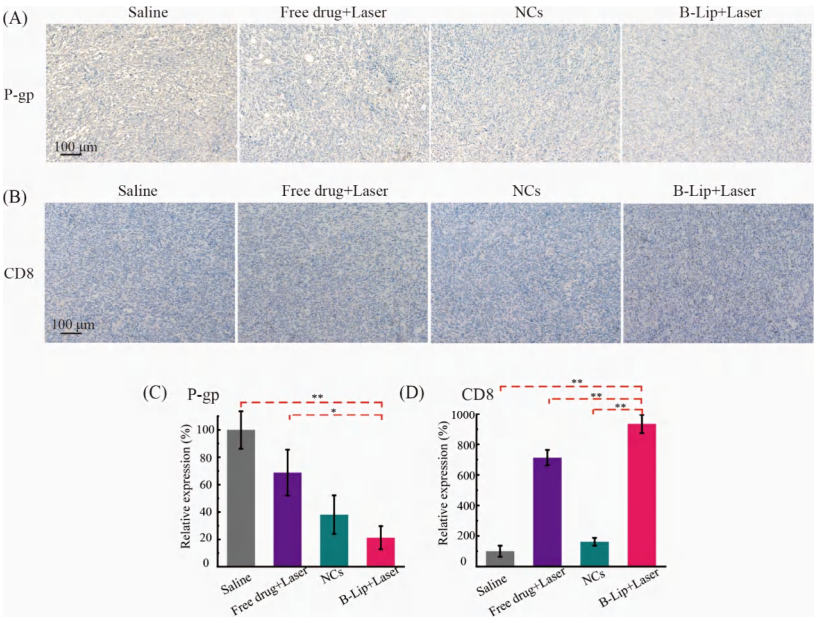

Figure 9. P-gp and CD8 in the tumor tissues of the Saline, Free drug (PTX, Cur, and Ce6 mixed solution)+Laser, PTX/Cur NCs (NCs), and B-Lip@PTX/Cur/Ce6 (B-Lip)+Laser groups in an antitumor detection assay in vivo tested by immunohistochemistry: representative micrographs of P-gp (A) and CD8 (B); quantified data of P-gp (C) and CD8 (D). $^{**}P < 0.001$ and $^{*}P < 0.05$.

tumor cells.[45] The activation of tumor-infiltrating lymphocytes (TILs) such as CD8+ T cells in tumor tissues correlates with smaller tumor size, reduced relapse rate, and improved overall survival. Immunohistochemical staining results of CD8 in the tumor tissues (Figure 9B) manifested that B-Lip@PTX/Cur/Ce6+Laser could provoke antitumor immunity by arousing T

https://doi.org/10.1021/acsanm.4c02669
ACS Appl. Nano Mater. XXXX, XXX, XXX−XXX

cell activation, as it significantly elevated the expression of CD8 in tumor tissues, which was also superior to Free drug+Laser ($P < 0.001$), PTX/Cur NCs ($P < 0.001$), and Saline ($P < 0.001$) (Figure 9D).

3.12. In Vivo and Ex Vivo Imaging. In vivo fluorescence imaging experiments demonstrated a significant and time-dependent accumulation of B-Lip@PTX/Cur/Ce6 in tumors following intravenous injection, with systemic visibility observed as early as 0.5 h and maximum fluorescence intensity achieved after 4 h of treatment (Figure 10A). Additionally, a robust

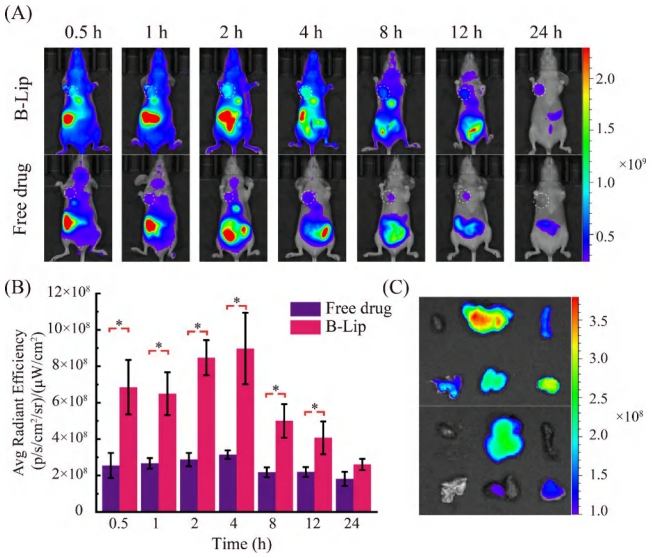

Figure 10. In vivo fluorescence imaging (A) and quantitative analysis of average fluorescence imaging signals for tumors (B) within BALB/c nude tumor bearing mice after intravenous injection of B-Lip@PTX/Cur/Ce6 (B-Lip) and Free drug (PTX, Cur, and Ce6 mixed solution) at 0.5, 1, 2, 4, 8, 12, and 24 h ($n = 5$). *$P < 0.05$. (C) Ex vivo images of major organs and tumors in mice 24 h after injection of B-Lip@PTX/Cur/Ce6 (B-Lip) and Free drug (PTX, Cur, and Ce6 mixed solution).

fluorescence signal was still observed at the tumor site up to 24 h postinjection, suggesting the specific retention of B-Lip@PTX/Cur/Ce6 at the tumor sites. B-Lip@PTX/Cur/Ce6 also demonstrated predominant accumulation in the liver and kidney, attributed to nonspecific uptake by reticuloendothelial cells. The fluorescence intensity signal at the tumor site was significantly higher in mice treated with B-Lip@PTX/Cur/Ce6 compared to those treated with Free drug ($P < 0.05$) at 0−12 h time points (Figure 10B). Free drug primarily accumulated in the liver, and that distributed in tumors rapidly disappeared, likely due to the limited tumor-targeting capability of small molecular dyes and their facile elimination in vivo. Collectively, the experimental findings demonstrated that B-Lip@PTX/Cur/Ce6 exhibited the capability to not only prolong the circulation duration of enclosed medications but also substantially augment the duration of drug accumulation at tumor sites. After the experiment, the in vitro fluorescence imaging of major organs, including heart, spleen, lung, and kidney, as well as tumor tissues, further substantiated that the fluorescence intensity at tumor sites in B-Lip@PTX/Cur/Ce6, following intravenous administration, surpassed that of Free drug (Figure 10C). These outcomes reaffirmed the robust tumor-targeting proficiency and protracted retention period within the tumor region of B-Lip@PTX/Cur/Ce6, with the enhanced tumor retention potentially attributed to the extended drug circulation facilitated by RBCEM. Briefly, the application of EM coating on the surface of B-Lip@PTX/Cur/Ce6 was found to enhance the biological compatibility of the nanodrug delivery system. The presence of CD47 protein on the RBCM enabled the system to effectively imitate the biological characteristics of the host cells, thereby evading phagocytosis by macrophages, transmitting a "do not eat me" signal to the host cells, and refraining from engulfing them.[46] Therefore, the increased distribution of B-Lip@PTX/Cur/Ce6 in tumor tissues could be attributed to the improved endocytosis of tumor cells facilitated by the encapsulation of RBCM on B-Lip@PTX/Cur/Ce6.

4. CONCLUSION

In this study, an erythrocyte membrane-camouflaged nanodrug delivery system capable of simultaneously loading PTX, Cur, and Ce6 was developed with the objective of overcoming MDR in breast cancer and achieving synergistic PDT and chemotherapy for cancer treatment. Both in vitro and in vivo experiments were conducted and verified the laser-responsive release profiles of B-Lip@PTX/Cur/Ce6, its ability to enhance tumor accumulation, its excellent antitumor efficacy, and its minimal side effects. Besides, results demonstrated that B-Lip@PTX/Cur/Ce6 could effectively deliver paclitaxel and curcumin to resistant cells while inhibiting P-gp function, thereby significantly enhancing the antitumor effects of PTX. Significantly, the application of laser irradiation effectively stimulated B-Lip@PTX/Cur/Ce6 to generate substantial intracellular ROS and facilitate photodynamic therapy. In summary, the designed B-Lip@PTX/Cur/Ce6 system demonstrated the ability to inhibit MDR and exhibit antitumor efficacy via chemo-photodynamic therapy. The potential therapeutic effects and underlying molecular mechanisms of this system provide a promising strategy for precise and effective treatment of MDR breast cancer in clinical applications.

■ ASSOCIATED CONTENT

Supporting Information

The Supporting Information is available free of charge at https://pubs.acs.org/doi/10.1021/acsanm.4c02669.

Thermodynamic parameters of PTX/Cur, half-maximal inhibitory concentration (IC_{50}) values, half-combination index (CI_{50}) values, and in vivo serum biochemical levels of different formulations, SDS-PAGE protein identification, UV−visible absorption and fluorescence spectra, storage stability investigation, TEM images, cellular uptake, and histological images obtained from main organs of different formulations (PDF)

■ AUTHOR INFORMATION

Corresponding Authors

Min Liu − *Institute of Biopharmaceutical Research, Liaocheng University, Liaocheng, Shandong 252059, People's Republic of China;* orcid.org/0000-0002-1918-9072;
Email: panpanliumin@163.com

Yanna Zhao − *Institute of Biopharmaceutical Research, Liaocheng University, Liaocheng, Shandong 252059, People's Republic of China;* orcid.org/0000-0001-9658-9996;
Email: ynzhao2011@163.com

https://doi.org/10.1021/acsanm.4c02669
ACS Appl. Nano Mater. XXXX, XXX, XXX−XXX

Authors

Qingran Guan − *Institute of Biopharmaceutical Research, Liaocheng University, Liaocheng, Shandong 252059, People's Republic of China*

Jianshuo Su − *Institute of Biopharmaceutical Research, Liaocheng University, Liaocheng, Shandong 252059, People's Republic of China*

Yinglan Li − *Institute of Biopharmaceutical Research, Liaocheng University, Liaocheng, Shandong 252059, People's Republic of China*

Huaizhen Zhang − *School of Geography and Environment, Liaocheng University, Liaocheng, Shandong 252059, People's Republic of China*

Zhuang Ding − *Institute of Biopharmaceutical Research, Liaocheng University, Liaocheng, Shandong 252059, People's Republic of China*

Qingpeng Wang − *Institute of Biopharmaceutical Research, Liaocheng University, Liaocheng, Shandong 252059, People's Republic of China;* orcid.org/0000-0002-2093-8237

Shilei Ji − *Institute of Biopharmaceutical Research, Liaocheng University, Liaocheng, Shandong 252059, People's Republic of China*

Jun Han − *Institute of Biopharmaceutical Research, Liaocheng University, Liaocheng, Shandong 252059, People's Republic of China*

Complete contact information is available at: https://pubs.acs.org/10.1021/acsanm.4c02669

Author Contributions

Q.G.: investigation, formal analysis, writing-original draft. J.S.: investigation, formal analysis. Y.L.: investigation, data curation. H.Z.: validation, formalanalysis. Z.D.: formal analysis, data curation. Q.W.: data curation, visualization. S.J.: formal analysis, data curation. J.H.: conceptualization, supervision. M.L.: project administration, supervision, funding acquisition. Y.Z.: conceptualization, methodology, project administration, visualization, writing-review and editing.

Author Contributions

[§]Q.G. and J.S. contributed equally.

Notes

The authors declare no competing financial interest.

■ ACKNOWLEDGMENTS

This work was financially supported by the National Natural Science Foundation of China (no. 22073039), the Natural Science Foundation of Shandong Province of China (no. ZR2022LSW018, no. ZR2020MB052, no. ZR2021QB198), and the Foundation of Liaocheng University (no. 318051522). This work was also technically supported by the Shandong Collaborative Innovation Center for Antibody Drugs, the Shandong Province Engineering Research Center for Nanomedicine and Drug Delivery Systems, and the Shandong Province Engineering Laboratory of Anti-Viral Drugs.

■ REFERENCES

(1) Miller, K. D.; Nogueira, L.; Devasia, T.; Mariotto, A. B.; Yabroff, K. R.; Jemal, A.; Kramer, J.; Siegel, R. L. Cancer treatment and survivorship statistics, 2022. *CA Cancer J. Clin* **2022**, *72* (5), 409−436.

(2) Zhan, Z.; Scala, S.; Monks, A.; Hose, C.; Bates, S.; Fojo, T. Resistance to paclitaxel mediated by P-glycoprotein can be modulated by changes in the schedule of administration. *Cancer Chemother Pharmacol* **1997**, *40* (3), 245−250.

(3) Zhan, X.; Nie, X.; Gao, F.; Zhang, C.; You, Y. Z.; Yu, Y. An NIR-activated polymeric nanoplatform with ROS- and temperature-sensitivity for combined photothermal therapy and chemotherapy of pancreatic cancer. *Biomater Sci.* **2020**, *8* (21), 5931−5940.

(4) Molavi, O.; Narimani, F.; Asiaee, F.; Sharifi, S.; Tarhriz, V.; Shayanfar, A.; Hejazi, M.; Lai, R. Silibinin sensitizes chemo-resistant breast cancer cells to chemotherapy. *Pharm. Biol.* **2017**, *55* (1), 729−739.

(5) Zhou, L.; Wang, H.; Li, Y. Stimuli-Responsive Nanomedicines for Overcoming Cancer Multidrug Resistance. *Theranostics* **2018**, *8* (4), 1059−1074.

(6) Wang, M.; Chen, W.; Chen, J.; Yuan, S.; Hu, J.; Han, B.; Huang, Y.; Zhou, W. Abnormal saccharides affecting cancer multi-drug resistance (MDR) and the reversal strategies. *Eur. J. Med. Chem.* **2021**, *220*, No. 113487.

(7) Zhang, Y.; Zhang, W.; Wang, Y.; Zhu, J.; Zhou, M.; Peng, C.; He, Z.; Sun, J.; Li, Z.; Gui, S. Emerging nanotaxanes for cancer therapy. *Biomaterials* **2021**, *272*, No. 120790.

(8) Ol'shevskaya, V. A.; Nikitina, R. G.; Savchenko, A. N.; Malshakova, M. V.; Vinogradov, A. M.; Golovina, G. V.; Belykh, D. V.; Kutchin, A. V.; Kaplan, M. A.; Kalinin, V. N.; Kuzmin, V. A.; Shtil, A. A. Novel boronated chlorin e6-based photosensitizers: Synthesis, binding to albumin and antitumour efficacy. *Bioorg. Med. Chem.* **2009**, *17* (3), 1297−1306.

(9) Liao, W.; Xiao, S.; Yang, J.; Shi, X.; Zheng, Y. Multifunctional nanogel based on carboxymethyl cellulose interfering with cellular redox homeostasis enhances phycocyanobilin photodynamic therapy. *Carbohydr. Polym.* **2024**, *323*, No. 121416.

(10) Agostinis, P.; Berg, K.; Cengel, K. A.; Foster, T. H.; Girotti, A. W.; Gollnick, S. O.; Hahn, S. M.; Hamblin, M. R.; Juzeniene, A.; Kessel, D.; Korbelik, M.; Moan, J.; Mroz, P.; Nowis, D.; Piette, J.; Wilson, B. C.; Golab, J. Photodynamic therapy of cancer: an update. *CA Cancer J. Clin* **2011**, *61* (4), 250−281.

(11) Wan, G.; Chen, B.; Li, L.; Wang, D.; Shi, S.; Zhang, T.; Wang, Y.; Zhang, L.; Wang, Y. Nanoscaled red blood cells facilitate breast cancer treatment by combining photothermal/photodynamic therapy and chemotherapy. *Biomaterials* **2018**, *155*, 25−40.

(12) Li, X.; Lovell, J. F.; Yoon, J.; Chen, X. Clinical development and potential of photothermal and photodynamic therapies for cancer. *Nat. Rev. Clin Oncol* **2020**, *17* (11), 657−674.

(13) Zhang, T.; Liu, H.; Li, L.; Guo, Z.; Song, J.; Yang, X.; Wan, G.; Li, R.; Wang, Y. Leukocyte/platelet hybrid membrane-camouflaged dendritic large pore mesoporous silica nanoparticles co-loaded with photo/chemotherapeutic agents for triple negative breast cancer combination treatment. *Bioact Mater.* **2021**, *6* (11), 3865−3878.

(14) Lin, J.; Li, D.; Li, C.; Zhuang, Z.; Chu, C.; Ostrikov, K.; Thompson, E. W.; Liu, G.; Wang, P. A review on reactive oxygen species (ROS)-inducing nanoparticles activated by uni- or multi-modal dynamic treatment for oncotherapy. *Nanoscale* **2023**, *15* (28), 11813−11833.

(15) Guan, Q.; Li, Y.; Zhang, H.; Liu, S.; Ding, Z.; Fan, Z.; Wang, Q.; Wang, Z.; Han, J.; Liu, M.; Zhao, Y. Laser-responsive multi-functional nanoparticles for efficient combinational chemo-photodynamic therapy against breast cancer. *Colloids Surf. B Biointerfaces* **2022**, *216*, No. 112574.

(16) Ma, Q.; Zhao, Y.; Guan, Q.; Zhao, Y.; Zhang, H.; Ding, Z.; Wang, Q.; Wu, Y.; Liu, M.; Han, J. Amphiphilic block polymer-based self-assembly of high payload nanoparticles for efficient combinatorial chemo-photodynamic therapy. *Drug Deliv* **2020**, *27* (1), 1656−1666.

(17) Tóth, S.; Szepesi, Á.; Tran-Nguyen, V. K.; Sarkadi, B.; Német, K.; Falson, P.; Di Pietro, A.; Szakács, G.; Boumendjel, A. Synthesis and Anticancer Cytotoxicity of Azaaurones Overcoming Multidrug Resistance. *Molecules* **2020**, *25* (3), 764.

(18) Assaraf, Y. G.; Brozovic, A.; Gonçalves, A. C.; Jurkovicova, D.; Linē, A.; Machuqueiro, M.; Saponara, S.; Sarmento-Ribeiro, A. B.; Xavier, C. P. R.; Vasconcelos, M. H. The multi-factorial nature of clinical multidrug resistance in cancer. *Drug Resist Updat* **2019**, *46*, No. 100645.

(19) Prasad, S.; Gupta, S. C.; Tyagi, A. K.; Aggarwal, B. B. Curcumin, a component of golden spice: from bedside to bench and back. *Biotechnol Adv.* **2014**, *32* (6), 1053−1064.
(20) Wei, Y.; Yang, P.; Cao, S.; Zhao, L. The combination of curcumin and 5-fluorouracil in cancer therapy. *Arch Pharm. Res.* **2018**, *41* (1), 1−13.
(21) Gupta, S. C.; Patchva, S.; Aggarwal, B. B. Therapeutic roles of curcumin: lessons learned from clinical trials. *Aaps j* **2013**, *15* (1), 195−218.
(22) Aggarwal, B. B.; Deb, L.; Prasad, S. Curcumin differs from tetrahydrocurcumin for molecular targets, signaling pathways and cellular responses. *Molecules* **2015**, *20* (1), 185−205.
(23) Ma, W.; Guo, Q.; Li, Y.; Wang, X.; Wang, J.; Tu, P. Co-assembly of doxorubicin and curcumin targeted micelles for synergistic delivery and improving anti-tumor efficacy. *Eur. J. Pharm. Biopharm* **2017**, *112*, 209−223.
(24) Villa, C. H.; Anselmo, A. C.; Mitragotri, S.; Muzykantov, V. Red blood cells: Supercarriers for drugs, biologicals, and nanoparticles and inspiration for advanced delivery systems. *Adv. Drug Deliv Rev.* **2016**, *106*, 88−103.
(25) Sun, D.; Chen, J.; Wang, Y.; Ji, H.; Peng, R.; Jin, L.; Wu, W. Advances in refunctionalization of erythrocyte-based nanomedicine for enhancing cancer-targeted drug delivery. *Theranostics* **2019**, *9* (23), 6885−6900.
(26) Wang, Y.; Zhang, K.; Qin, X.; Li, T.; Qiu, J.; Yin, T.; Huang, J.; McGinty, S.; Pontrelli, G.; Ren, J.; Wang, Q.; Wu, W.; Wang, G. Biomimetic Nanotherapies: Red Blood Cell Based Core-Shell Structured Nanocomplexes for Atherosclerosis Management. *Adv. Sci. (Weinh)* **2019**, *6* (12), No. 1900172.
(27) Gao, M.; Liang, C.; Song, X.; Chen, Q.; Jin, Q.; Wang, C.; Liu, Z. Erythrocyte-Membrane-Enveloped Perfluorocarbon as Nanoscale Artificial Red Blood Cells to Relieve Tumor Hypoxia and Enhance Cancer Radiotherapy. *Adv. Mater.* **2017**, *29* (35), No. 1701429.
(28) Wang, Y.; Chen, X.; He, D.; Zhou, Y.; Qin, L. Surface-Modified Nanoerythrocyte Loading DOX for Targeted Liver Cancer Chemotherapy. *Mol. Pharmaceutics* **2018**, *15* (12), 5728−5740.
(29) Luk, B. T.; Hu, C. M.; Fang, R. H.; Dehaini, D.; Carpenter, C.; Gao, W.; Zhang, L. Interfacial interactions between natural RBC membranes and synthetic polymeric nanoparticles. *Nanoscale* **2014**, *6* (5), 2730−2737.
(30) Hu, C. M.; Zhang, L.; Aryal, S.; Cheung, C.; Fang, R. H.; Zhang, L. Erythrocyte membrane-camouflaged polymeric nanoparticles as a biomimetic delivery platform. *Proc. Natl. Acad. Sci. U. S. A.* **2011**, *108* (27), 10980−10985.
(31) Fang, R. H.; Hu, C. M.; Chen, K. N.; Luk, B. T.; Carpenter, C. W.; Gao, W.; Li, S.; Zhang, D. E.; Lu, W.; Zhang, L. Lipid-insertion enables targeting functionalization of erythrocyte membrane-cloaked nanoparticles. *Nanoscale* **2013**, *5* (19), 8884−8888.
(32) Zhao, Y.; Cai, C.; Liu, M.; Zhao, Y.; Wu, Y.; Fan, Z.; Ding, Z.; Zhang, H.; Wang, Z.; Han, J. Drug-binding albumins forming stabilized nanoparticles for co-delivery of paclitaxel and resveratrol: In vitro/in vivo evaluation and binding properties investigation. *Int. J. Biol. Macromol.* **2020**, *153*, 873−882.
(33) Wani, T. A.; Bakheit, A. H.; Ansari, M. N.; Al-Majed, A. A.; Al-Qahtani, B. M.; Zargar, S. Spectroscopic and molecular modeling studies of binding interaction between bovine serum albumin and roflumilast. *Drug Des Devel Ther* **2018**, *12*, 2627−2634.
(34) Zhao, Z.; Meng, H.; Wang, N.; Donovan, M. J.; Fu, T.; You, M.; Chen, Z.; Zhang, X.; Tan, W. A controlled-release nanocarrier with extracellular pH value driven tumor targeting and translocation for drug delivery. *Angew. Chem., Int. Ed. Engl.* **2013**, *52* (29), 7487−7491.
(35) Liu, M.; Liu, T.; Shi, Y.; Zhao, Y.; Yan, H.; Sun, B.; Wang, Q.; Wang, Z.; Han, J. Comparative study on the interaction of oxyresveratrol and piceatannol with trypsin and lysozyme: binding ability, activity and stability. *Food Funct* **2019**, *10* (12), 8182−8194.
(36) Verma, A.; Guha, S.; Diagaradjane, P.; Kunnumakkara, A. B.; Sanguino, A. M.; Lopez-Berestein, G.; Sood, A. K.; Aggarwal, B. B.; Krishnan, S.; Gelovani, J. G.; Mehta, K. Therapeutic significance of elevated tissue transglutaminase expression in pancreatic cancer. *Clin. Cancer Res.* **2008**, *14* (8), 2476−2483.
(37) Wani, T. A.; Bakheit, A. H.; Al-Majed, A. A.; Altwaijry, N.; Baquaysh, A.; Aljuraisy, A.; Zargar, S. Binding and drug displacement study of colchicine and bovine serum albumin in presence of azithromycin using multispectroscopic techniques and molecular dynamic simulation. *J. Mol. Liq.* **2021**, *333*, No. 115934.
(38) Wang, W.; Xi, M.; Duan, X.; Wang, Y.; Kong, F. Delivery of baicalein and paclitaxel using self-assembled nanoparticles: synergistic antitumor effect in vitro and in vivo. *Int. J. Nanomedicine* **2015**, *10*, 3737−3750.
(39) Zhao, Y.; Cai, C.; Liu, M.; Zhao, Y.; Pei, W.; Chu, X.; Zhang, H.; Wang, Z.; Han, J. An organic solvent-free technology for the fabrication of albumin-based paclitaxel nanoparticles for effective cancer therapy. *Colloids Surf. B Biointerfaces* **2019**, *183*, No. 110394.
(40) Ma, P.; Chen, J.; Bi, X.; Li, Z.; Gao, X.; Li, H.; Zhu, H.; Huang, Y.; Qi, J.; Zhang, Y. Overcoming Multidrug Resistance through the GLUT1-Mediated and Enzyme-Triggered Mitochondrial Targeting Conjugate with Redox-Sensitive Paclitaxel Release. *ACS Appl. Mater. Interfaces* **2018**, *10* (15), 12351−12363.
(41) Lin, X.; Wang, Q.; Du, S.; Guan, Y.; Qiu, J.; Chen, X.; Yuan, D.; Chen, T. Nanoparticles for co-delivery of paclitaxel and curcumin to overcome chemoresistance against breast cancer. *J. Drug Deliv Sci. Technol.* **2023**, *79*, No. 104050.
(42) Luo, L.; Qi, Y.; Zhong, H.; Jiang, S.; Zhang, H.; Cai, H.; Wu, Y.; Gu, Z.; Gong, Q.; Luo, K. GSH-sensitive polymeric prodrug: Synthesis and loading with photosensitizers as nanoscale chemo-photodynamic anti-cancer nanomedicine. *Acta Pharm. Sin B* **2022**, *12* (1), 424−436.
(43) Cuellar-Núñez, M. L.; Gonzalez de Mejia, E.; Loarca-Piña, G. Moringa oleifera leaves alleviated inflammation through down-regulation of IL-2, IL-6, and TNF-α in a colitis-associated colorectal cancer model. *Food Res. Int.* **2021**, *144*, No. 110318.
(44) Wu, Z.-L.; Chen, Y.; Qu, Z.; Wu, G.-Y.; He, X.-F.; Huang, J.-W.; Meng, Q.-Q.; Hu, Y.-H.; Shen, X.-L.; Yang, R.-Y.; Hu, Y.-J. An ester derivative of tenacigenin B from Marsdenia tenacissima (Roxb.) Wight et Arn reversed paclitaxel-induced MDR in vitro and in vivo by inhibiting both P-gp and MRP2. *J. Ethnopharmacol* **2022**, *294*, No. 115353.
(45) Li, H.; Feng, Y.; Luo, Q.; Li, Z.; Li, X.; Gan, H.; Gu, Z.; Gong, Q.; Luo, K. Stimuli-activatable nanomedicine meets cancer theranostics. *Theranostics* **2023**, *13* (15), 5386−5417.
(46) Xuan, M.; Shao, J.; Zhao, J.; Li, Q.; Dai, L.; Li, J. Magnetic Mesoporous Silica Nanoparticles Cloaked by Red Blood Cell Membranes: Applications in Cancer Therapy. *Angew. Chem., Int. Ed. Engl.* **2018**, *57* (21), 6049−6053.

https://doi.org/10.1021/acsanm.4c02669
ACS Appl. Nano Mater. XXXX, XXX, XXX−XXX